Supporting Material

Methods

Animal care

This study was approved by the Norwegian National Committee for Animal Welfare under the Norwegian Animal Welfare Act, which conforms to the *Guide for the Care and Use of Laboratory Animals* published by the US National Institutes of Health (NIH publication No. 85-23, revised 1996). Inducible, cardiomyocyte-specific disruption of the *Serca2* gene was attained by employing *Serca2*$^{flox/flox}$ Tg(αMHC-MerCreMer) mice (KO) (1). Gene excision in 8-10 week old mice was accomplished by inclusion of tamoxifen powder (RM1 FG SQC, 811004, Scanbur BK) in the feed (100 mg/200 g) for 7 days (2, 3). *Serca2*$^{flox/flox}$ mice (FF) served as controls (1, 4). Tamoxifen treatment results in Serca2 gene excision exclusively in the cardiomyocytes of KO animals (1). Hearts were harvested at 4 and 7 weeks following tamoxifen administration.

Cardiomyocyte experiments

Cardiomyocytes were isolated by retrograde perfusion of the heart with enzyme-containing solutions (1, 5). Isolated cells were then plated on laminin-coated coverslips and placed in a perfusion chamber on the stage of an inverted microscope. Intracellular $[Ca^{2+}]_i$ was measured in myocytes loaded with fluo-4 AM (Invitrogen Molecular Probes, Eugene, OR, USA). Diastolic $[Ca^{2+}]_i$ levels were first measured in cardiomyocytes pipette-loaded with fura-2. These mean values were then used to calibrate the $[Ca^{2+}]_i$ transients measured in fluo-4 loaded cells, as previously described (3). $[Ca^{2+}]_i$ transients were elicited by field stimulation (3 ms biphasic pulse, 25% above threshold) during perfusion with HEPES Tyrode solution containing (in mmol/L): 140 NaCl, 1 $CaCl_2$, 0.5 $MgCl_2$, 5.0 HEPES, 5.5 glucose, 0.4 NaH_2PO_4 and 5.4 KCl (pH 7.4, 37°C). In these experiments, an LSM 510 microscope (Zeiss GmbH, Jena, Germany) was used to record $[Ca^{2+}]_i$ transients in line-scan mode (6).

SR function was assessed by whole-cell fluorescence (Photon Technology International, Monmouth Junction, NJ, USA) recordings of intracellular $[Ca^{2+}]_i$. SR Ca^{2+} content was estimated by rapidly switching to an extracellular solution containing 10 mmol/L caffeine and measuring the magnitude of the elicited Ca^{2+} release. The SR-dependent component of the $[Ca^{2+}]_i$ transient was calculated by comparing the magnitude of $[Ca^{2+}]_i$ transients in the presence and absence of caffeine. The difference in the declining phase of the $[Ca^{2+}]_i$ transient under these two conditions was used to estimate rate constants for $[Ca^{2+}]_i$ re-uptake (SERCA activity) and extrusion (7). The contribution of NCX and PMCA to Ca^{2+} extrusion was estimated by comparing the declining phase of caffeine-elicited $[Ca^{2+}]_i$ transients in the presence and absence of 5 mmol/L Ni^{2+}.

Patch-clamp experiments were conducted with an Axoclamp 2B amplifier (Axon Instruments, Foster City, CA, USA), pCLAMP software (Axon Instruments), and low resistance pipettes (1-2 MΩ). APs were triggered by injecting a 3-ms depolarizing current in cells patch-clamped with a pipette solution containing (in mmol/L): 120 K-aspartate, 0.5 $MgCl_2$, 6 NaCl, 0.06 EGTA, 10 HEPES, 10 glucose, 25 KCl, and 4 K2-ATP (pH 7.2). L-type Ca^{2+} current was elicited by 200 ms voltage steps from -50 mV to a range of potentials, with an internal solution containing (in mmol/L) 130 CsCl, 0.33 $MgCl_2$, 4 Mg-ATP, 0.06 EGTA, 10 HEPES, and 20 TEA, and an extracellular solution containing (in mmol/L) 20 CsCl, 1 $MgCl_2$, 135 NaCl, 10 Hepes, 10 D-glucose, 4 4-aminopyridine, and 1 $CaCl_2$ (1, 3). Na^+/K^+-ATPase (NKA) currents were obtained by elevating extracellular $[K^+]$ from 0 mmol/L to 5.4 mmol/L, and contributions of the α_1 and α_2 NKA isoforms were distinguished based on differential sensitivity to ouabain bloackade (3, 8).

Intracellular $[Na^+]$ was assessed in cells loaded with SBFI AM (Invitrogen Molecular Probes, Eugene, OR, USA) using whole-cell photometry, and the fluorescence signal was calibrated to obtain $[Na^+]_i$ levels as described previously (8). Intracellular pH was determined by confocal microscopy in

cells loaded with SNARF-1 AM (Invitrogen). SNARF was excited at 543 nm, and pH was calculated from the ratio of fluorescence at 580 and 640 nm using a calibration curve obtained in permeabilized cells.

Statistics

Cardiomyocyte data are expressed as mean values ± SEM. Statistical significance was calculated using paired or unpaired t-tests, and P values <0.05 were considered significant.

Model Implementation

Justification for the addition of a subsarcolemmal compartment

Previously, we presented a mathematical modelling study of Ca^{2+} dynamics in the FF and 4-week KO cardiomyocytes (9). In that study, the FF and 4-week KO models were developed using a framework (10) which does not include the sub-sarcolemmal compartment and will be referred to as the lumped framework (the cytosolic and sub-sarcolemmal spaces were lumped into one cytosolic space). In the lumped framework, all transmembrane currents are uniformly distributed and most Ca^{2+} handling proteins such as NCX and PMCA are regulated by cytosolic Ca^{2+} concentration. This framework enabled parameterization of Ca^{2+} handling mechanisms as explicit functions of $[Ca^{2+}]_i$ and simulated Ca^{2+} dynamics were found to be in good agreement with experimental observations. However, during parameterization of the 7-week KO model, the simulated $[Ca^{2+}]_i$ transient using the lumped framework was significantly higher than experimental measurements. We then carried out detailed calculations of Ca^{2+} influx and efflux combined with thermodynamics consideration of NCX function as presented below. Such analysis revealed that, while it is sufficient to model the FF and 4-week KO using the lumped framework, a more detailed model of Ca^{2+} handling with a sub-sarcolemmal space was required to model the 7-week KO.

During a $[Ca^{2+}]_i$ transient, peak $[Ca^{2+}]_i$ is reached within approximately 40 ms and the size of a $[Ca^{2+}]_i$ transient ($\Delta[Ca^{2+}]_i$) is determined by the net Ca^{2+} influx during this initial period as well as intracelular Ca^{2+} buffering properties. The net Ca^{2+} influx can in turn be calculated as the difference between total Ca^{2+} entry through LCCs and SR Ca^{2+} release, and Ca^{2+} removal through SERCA, NCX and PMCA. In the FF cardiomyocytes, assuming most of the Ca^{2+} entry and SR Ca^{2+} release occur within the first 40 ms of the cardiac cycle, Ca^{2+} entry through LCCs could be estimated from the integral of the LCC current (I_{CaL}) recorded during an AP clamp (0.096 pC/pF), yielding approximately 3.3 μmol/L of Ca^{2+}. SR Ca^{2+} release could be estimated from the integral of SR Ca^{2+} uptake since Ca^{2+} release and uptake must be balanced over each cardiac cycle. Using the experimentally recorded $[Ca^{2+}]_i$ transient and fitted parameter values for SERCA to approximate and integrate the time course of Ca^{2+} uptake, the estimated total SR Ca^{2+} release and SR Ca^{2+} uptake during the first 40 ms were 37.7 and 4.4 μmol/L, respectively, yielding a net SR Ca^{2+} release of 33.3 μmol/L. Therefore, without taking into account of Ca^{2+} extrusion through NCX and PMCA during the first 40 ms, the net Ca^{2+} influx had an estimated value of 36.6 μmol/L.

On the other hand, given the observed $[Ca^{2+}]_i$ transient in the FF cardiomyocytes, the actual increase in the total concentration of Ca^{2+} ($\Delta[Ca^{2+}]_{tot}$) can be calculated as:

$$\Delta[Ca^{2+}]_{total} = \left(\frac{B_{max} \cdot [Ca^{2+}]_p}{K_d + [Ca^{2+}]_p} + [Ca^{2+}]_p\right) - \left(\frac{B_{max} \cdot [Ca^{2+}]_d}{K_d + [Ca^{2+}]_d} + [Ca^{2+}]_d\right) \quad (1)$$

where B_{max} and K_d denote the total concentration and Ca^{2+} affinity of buffers, respectively. $[Ca^{2+}]_p$ and $[Ca^{2+}]_d$ are the peak and diastolic $[Ca^{2+}]_i$, respectively. With a diastolic $[Ca^{2+}]_i$ of 0.113 ± 0.025 μmol/L, a $\Delta[Ca^{2+}]_i$ of 0.343 ± 0.065 μmol/L, and estimated B_{max} and K_d values of 109 and 0.6 μmol/L, respectively, $\Delta[Ca^{2+}]_{tot}$ was calculated to be between 24.3 and 35.4 μmol/L. The above calcu-

lations demonstrated that the net Ca^{2+} influx, without taking into account of Ca^{2+} extrusion, was close to the actual $\Delta[Ca^{2+}]_{tot}$ required. This makes it possible to use the lumped model framework for the FF model, in which NCX and PMCA sense cytosolic Ca^{2+} concentration and only a small amount of Ca^{2+} extrusion occurs during the first 40 ms.

Similar calculations were carried out with the 4-week and 7-week KO data. It was found that, in the 4-week KO, the net Ca^{2+} influx (13.7 μmol/L) was close to the actual $\Delta[Ca^{2+}]_{tot}$ (7.63 - 13.62 μmol/L). However, this was the not the case for the 7-week KO, in which there was a significant mismatch between net Ca^{2+} influx (13.87 μmol/L) and $\Delta[Ca^{2+}]_{tot}$ required (5.09 - 7.38 μmol/L), suggesting additional Ca^{2+} removal through trans-sarcolemmal Ca^{2+} extrusion.

Ca^{2+} extrusion through NCX is thermodynamically favoured when the Nernst potential of the exchanger (E_{NCX}) is more positive than the transmembrane potential (V_m). E_{NCX} is in turn governed by the equilibrium potentials for Ca^{2+} (E_{Ca}) and Na^+ (E_{Na}). When the lumped framework was used, E_{NCX} could be calculated as:

$$\begin{aligned} E_{NCX} &= 3E_{Na} - 2E_{Ca} \\ E_{Na} &= \frac{RT}{F} \cdot \ln\frac{[Na^+]_o}{[Na^+]_i} \\ E_{Ca} &= \frac{RT}{2F} \cdot \ln\frac{[Ca^{2+}]_o}{[Ca^{2+}]_i} \end{aligned} \tag{2}$$

where R is the universal gas constant (8.314 J·mol^{-1} ·K^{-1}), T is the absolute temperature (310 K), $[Ca^{2+}]_o$, $[Ca^{2+}]_i$, $[Na^+]_i$ and $[Na^+]_o$ are the intra-and extra-cellular ion concentrations. Using the experimentally measured $[Na^+]_i$ levels and $[Ca^{2+}]_i$ transients, E_{Na} and E_{Ca} during the first 40 ms of the cardiac cycle were estimated, as shown in Fig. S1A, for the FF, 4-week KO and 7-week KO. It can be seen that E_{Na} was similar between the FF and 4-week KO, but decreased significantly in the 7-week KO compared to the FF level, due to the 5 mmol/L elevation in $[Na^+]_i$. On the other hand, the decrease in the $[Ca^{2+}]_i$ transient led to a gradual rise in E_{Ca}. The resulting E_{NCX} and APs reconstructed from the average recorded APDs (APD_{20} APD_{50} and APD_{70}) are shown in Fig. S1B. The shaded areas where E_{NCX} is below V_m indicate the duration of NCX in reverse mode. For the FF and 4-week KO, NCX operated in forward Ca^{2+} extrusion mode during most of the 40 ms. However, for the 7-week KO, NCX operated in reverse mode during most of the 40 ms, as a result of both the decrease in E_{NCX} and the prolonged AP. This meant that using the lumped framework, there was little Ca^{2+} extrusion during the first 40 ms of the cardiac cycle as governed by the thermodynamics of the exchanger, such that total Ca^{2+} influx exceeded the actual $\Delta[Ca^{2+}]_{tot}$. As a result, simulated $[Ca^{2+}]_i$ transient would inevitably be greater than that observed experimentally.

The above analysis thus motivated the addition of subsarcolemmal space, so the transmembrane proteins sense ion concentrations in their respective sub-spaces. In this framework, $[Ca^{2+}]_i$ transient in the 7-week KO can be accurately matched as $[Ca^{2+}]_{jc}$ and $[Ca^{2+}]_{sl}$ rise much faster and higher than $[Ca^{2+}]_i$ thus driving NCX into the Ca^{2+} extrusion mode much earlier (see Fig.S2).

A subsarcolemmal compartment was thus incorporated into the previously developed mathematical framework of Ca^{2+} dynamics and APs in murine ventricular myocytes (10), following the approach of Shannon et al. (11). Such addition allowed differentially distributed proteins in the cell membrane to sense ion concentrations in their respective sub-spaces that could be substantially different from the bulk cytosolic concentrations during an AP, as shown in Fig. S2. Since the formulation of Shannon et al. (11) was originally developed for rabbit ventricular myocytes, some modifications were made based on experimental data from mice and rats. These include changes to the geometrical parameters, diffusion parameters and distribution of the ion channels, as explained below.

Geometrical considerations

The cell membrane was divided into two areas: the junctional membrane (A_{jc}), i.e. the area occupied by transverse tubules (T-tubules), and the surface sarcolemmal area (A_{sl}). The percentage area of the junctional membrane was determined based on a study by Page and Surdyk-Droske (12), which showed that in the mouse heart, on average 6% of the surface sarcolemma and 40% of the T-tubules are involved in junctional complexes. As a result, 19% of the cell membrane is junctional, with approximately 80% of which located in the T-tubules. Therefore, in our model the percentage area of the junctional membrane was set to 19%. For the differential distributions of the channels such as NCX and NKA (see later), we have assumed that their maximal conductances in the junctional membrane are the same as those measured in the T-tubules, since the majority of the junction complexes are located in the T-tubules. Similarly, we have also assumed that the maximal conductances of these channels in the surface sarcolemma are the same as those measured in detubulated membranes, since the majority of the surface sarcolemma is not in the T-system.

The cell volume (2.2×10^{-5} μL) (13) was separated into five compartments, four of which (junctional space (jc or dyadic space ds), junctional SR (JSR), network SR (NSR) and the cytosolic space (cyt)) have been described previously (10). An additional subsarcolemmal space (sl), located directly underneath the surface sarcolemma area and occupying 2% of the cell volume, was added to the model.

Diffusion parameters

Following the approach of Shannon et al. (11), the rate of diffusion of ions (Na^+ and Ca^{2+}) from space jc to space sl was defined as:

$$J_{I_{jcsl}} = D_{I_{jcsl}} \cdot A_{jcsl} \cdot \frac{[I]_{jc} - [I]_{sl}}{\Delta x_{jcsl}} \tag{3}$$

where $D_{I_{jcsl}}$ is the diffusion coefficient for the ion, A_{jcsl} is the interface area between the junction space and the subsarcolemmal space, Δx_{jcsl} is the distance between the centres of the two compartments, and $[I]_{jc} - [I]_{sl}$ is the difference in ion concentrations.

Similarly, the rate of diffusion of ions from space sl to space cyt was defined as:

$$J_{I_{slcyt}} = D_{I_{slcyt}} \cdot A_{slcyt} \cdot \frac{[I]_{sl} - [I]_{i}}{\Delta x_{slcyt}} \tag{4}$$

The diffusion coefficients for Na^+ and Ca^{2+} ions in equations 3 and 4 were set to the same values as those in the Shannon et al. model (11), as listed in Table S3. The diffusion distances and interface areas were adjusted from the values used by Shannon et al., according to the differences in geometry, as explained below.

Each junction was considered to be a disk with a radius of 0.16 μm with a height of 0.015 μm (11). The cross-sectional area is therefore 0.08 μm^2. Given that A_{jc} is equal to 2800 μm^2 (19% of A_{tot}), the total number of junctions is thus approximately 35150. This yielded an even spacing of 0.986 μm between junctions, which is 18% smaller compared to the 1.2 μm spacing in the Shannon et al. model. Therefore, the distance of diffusion to the middle of the SL compartment was reduced by 35% from 0.5 to 0.41 μm (See Fig 1.B in ref. (11)). The side area of a junction is 0.015 μm^2, giving a total interface area of 5.27×10^{-6} cm^2 for diffusion from junctional space to subsarcolemmal space.

The distance of diffusion from the subsarcolemmal space to the cytosol was kept unchanged from the value used by Shannon et al. (0.45 μm), and the interface area was approximated by the area of the surface sarcolemma (1.2×10^{-4} cm^2, 81% of A_{tot}).

The addition of the subsarcolemmal compartment with the aforementioned Ca^{2+} diffusion parameters resulted in an approximately ten-fold increase in the magnitude of $[Ca^{2+}]_{jc}$, compared to the lumped model. However, coorperative binding of Ca^{2+} to RyR with a hill coefficient of 4 for transition from state C_1 to state O_1 and 3 for transition from state O_1 to state O_2 in the model meant that the resulting forward rate constants would be approximately 10^4 and 10^3 times faster, respectively. This resulted in a significantly prolonged opening time of the RyRs and instability of the model (the proportion of RyRs in state C dropped transiently to just below zero in some simulations). We therefore adjusted the

Ca^{2+}-sensitivity of the RyR to ensure the proper functioning of the channel, as suggested by Jafri et al. (14).

K^+ ion dynamics were not compartmentalized, following the approach of Shannon et al. (11).

Differential distribution of transmembrane ion channels

In adult mouse heart, two isoforms of the Na^+/K^+-ATPase α-subunit (α_1 and α_2) have been found, which are distributed differentially in the T-tubule and surface sarcolemmal membranes. In the study by Berry et al. (15), preferential inhibition of the high ouabain affinity α_2 subunits in control and detubulated mouse ventricular myocytes revealed that the current densities of $I_{NKA,\alpha1}$ and $I_{NKA,\alpha2}$ in the T-tubules are 1.37 and 5.57 times greater, respectively, than those in the surface sarcolemma. In our model, $I_{NKA,\alpha1}$ and $I_{NKA,\alpha2}$ were computed separately, and the data by Berry et al. (15) were used to define the maximum $I_{NKA,\alpha1}$ and $I_{NKA,\alpha2}$ in the junctional and sarcolemma areas in the model ($I^{max}_{NKA,\alpha1}$(jc) = 1.276·$I^{max}_{NKA,\alpha1}$, $I^{max}_{NKA,\alpha1}$(sl) = 0.931 ·$I^{max}_{NKA,\alpha1}$, $I^{max}_{NKA,\alpha2}$(jc) = 2.98 ·$I^{max}_{NKA,\alpha2}$, $I^{max}_{NKA,\alpha2}$(sl) = 0.535· $I^{max}_{NKA,\alpha2}$).

The current density of NCX in the junctinal membrane was found to be three times greater than that in the surface sarcolemma, based on I_{NCX} measurements from detubulated rat ventricular myocytes (16). Yang et al. (17) also found very little NCX current in detubulated rat ventricular myocytes, indicating the majority of the channels are located on the T-tubules. Therefore, the maximum NCX activity on the junctional membrane was set to be three times greater than on the surface sarcolemma (V^{max}_{NCX}(jc) = 2.175·V^{max}_{NCX}, V^{max}_{NCX}(sl) = 0.725·V^{max}_{NCX}).

The distribution of LCCs has been assessed by Scriven et al. (18) in rat ventricular myocytes. Using indirect immunofluorescence, it was found that the majority of the LCCs are located on the T-tubules, with very little immunolabelling on the surface sarcolemma. In another study in rat ventricular myocytes (19), detubulation revealed that LCC density is 8.7 times greater on the T tubules than on the surface membrane (P_{CaL}(sl) = 0.1·P_{CaL}(jc). Therefore, in our model, the permeability of the channels on the junctional membrane is nine times greater than on the surface sarcolemma. It was also assumed in the model that, Ca^{2+}-induced-Ca^{2+} release is only triggered by Ca^{2+} entry through the LCCs located on the junctional membrane.

The distribution of the fast Na^+ channels on the cell membrane was assumed to be uniform in our model, consistent with the observations by two different groups (20, 17), both in rat ventricular myocytes. The distribution of plasmamembrane Ca^{2+} ATPase (PMCA) is currently unknown, although Ca^{2+} extrusion through PMCA was found to be present in detubulated rat ventricular myocytes (17). This protein was thus assumed to be uniformly distributed on the cell membrane. Relatively few studies have been carried out on the distribution of K^+ channels, which were also assumed to be uniformly distributed.

Buffering

Ca^{2+} buffering parameters in the junctional space, cytosolic space and the SR were kept the same as those in our previous model (10). Buffering parameters for the additional subsarcolemmal space were the same as those used in the junctional and cytosolic spaces.

Experimental data on Na^+ buffering is sparse, although in one study (21) in rabbit ventricular myocytes Na^+ buffering capacity has been reported to be very low (approximately 1.3). In our model, Na^+ buffering was included following the same formulations and parameter values as those in the Shannon et al. model (11).

Model Parameterization

The Na^+/K^+-ATPase (FF and 4-week KO)

In the current study, I_{NKA} in the FF and 7-week KO cardiomycytes were measured in dialyzed cells

($[Na^+]_i$ = 50 mmol/L) under whole-cell voltage clamping at -50 mV holding potential. The current was activated by switching from a K^+-free to K^+-containing external solution (5.4 mmol/L $[K^+]_o$), and $I_{NKA,\alpha1}$ and $I_{NKA,\alpha2}$ were differentiated using ouabain which blocks the α_2 isoform.

Before fitting the NKA formulations to our I_{NKA} measurements, a range of existing experimental data from mice, and in some cases rats, were used to define the voltage- and $[Na^+]_i$-dependent properties of the current. The voltage-dependence of $I_{NKA,\alpha1}$ and $I_{NKA,\alpha2}$ was parameterized to experimental measurements by Swift et al. (8) in rat ventricular myocytes at 37 ^oC, as shown in Fig. S3. The activation of NKA by intracellular Na^+ has been studied by various groups, and a wide range of values for the affinity constant (K_m) have been reported. For example, the mean K_m values for rat ventricular myocytes at physiological temperatures range from 10.2 mmol/L (21), 17.0 mmol/L (16) to 40 mmol/L (22). These differences may, at least partially, be explained by variations in actual subsarcolemmal $[Na^+]$ which may not always be accurately controlled by the $[Na^+]$ in the pipette solution. In normal mouse ventricular myocytes, Berry et al. (15) measured total, α_1 and α_2-mediated Na^+ effluxes as a function of $[Na^+]_i$ at 35 ^oC. The Na^+ affinity of the total NKA function was equal to 16.6 $\pm$ 0.2 mmol/L with similar K_m values for the α_1 and α_2 subunits (16.6 $\pm$ 0.8 and 16.7 $\pm$ 2.6 mmol/L, respectively). The hill coefficient (nh) of total NKA function was equal to 2.3 $\pm$ 0.1, with values of 2.3 $\pm$ 0.1 and 4.1 $\pm$ 0.8, for the α_1 and α_2 subunits, respectively. In another study, Han et al. (23) reported a K_m of 18.3 $\pm$ 2.7 mmol/L and an nh of 2.8 $\pm$ 0.2 for the overall NKA function in mouse ventricular myocytes at room temperature.

Based on the experimental evidence above, the K_m and nh values for the α_1 and α_2 subunits were set to be equal in the FF model. Various combinations of K_m and nh values within the range of experimental data were then tested in whole cell simulations and the resulting $[Na^+]_i$ levels compared with experimentally observed level in FF cardiomyocytes ($[Na^+]_i$ = 9.6 $\pm$ 1.4 mmol/L). For each combination, we first parameterized $I^{max}_{NKA,\alpha1}$ and $I^{max}_{NKA,\alpha2}$ based on our measurements of $I_{NKA,\alpha1}$ (2.61 $\pm$ 0.10 pA/pF) and $I_{NKA,\alpha2}$ (0.81 $\pm$ 0.09 pA/pF) in dialyzed cells at -50 mV. The models of α_1 and α_2 NKA isoforms were then incorporated into the previously developed model framework (10) for simulations of $[Na^+]_i$ under field-stimulations at 1 Hz. As shown in Fig. S4, experimentally measured $[Na^+]_i$ value was only matched with high nh and high K_m values. For this reason, we set nh to 3 and K_m to 21 mmol/L in our model, with fitted $I^{max}_{NKA,\alpha1}$ and $I^{max}_{NKA,\alpha2}$ equal to 5.2 and 1.95 pA/pF, respectively. NKA parameters for the 4-week KO model were kept identical to those in the FF model.

The Na^+/K^+-ATPase (7-week KO)

In 7-week KO cardiomyocytes, $I_{NKA,\alpha1}$ and $I_{NKA,\alpha2}$ during voltage-clamp experiments were decreased from their FF values of 2.61 $\pm$ 0.10 and 0.81 $\pm$ 0.09 pA/pF, respectively, to 2.35 $\pm$ 0.10 and 0.45 $\pm$ 0.06 pA/pF, respectively. At the same time, $[Na^+]_i$ level during 1 Hz field-stimulation was also higher (14.6 $\pm$ 1.1 mmol/L) compared to the FF (9.6 $\pm$ 1.4 mmol/L), which was initially thought to result only from NKA down-regulation. However, when $I^{max}_{NKA,\alpha1}$ and $I^{max}_{NKA,\alpha1}$ were fitted to experimental measurements ($I^{max}_{NKA,\alpha1}$(7-week KO) = 4.4 pA/pF and $I^{max}_{NKA,\alpha2}$ (7-week KO) = 0.9 pA/pF), simulated $[Na^+]_i$ under 1 Hz field-stimulations was increased by about 2 mmol/L compared to the FF value, as shown in Fig. S4.

Na^+ accumulation in HF has been associated with increases in Na^+ influx such as the persistent Na^+ current in some studies. We thus used our model to test whether increases in the fast and persistent Na^+ currents can explain the additional increase in $[Na^+]_i$ seen in the KO. With J_{acid} = 0 μM/ms, the conductivity of the fast Na^+ current (G_{Na}) was increased from its original value of 16 pA/pF to a maximum value of 23 pA/pF. G_{Na} could not be increased beyond 23 pA/pF as the Na^+ channel model includes both the fast and persistent channel kinetics (24), and the increased persistent current at higher G_{Na} values prevented the cell model from repolarising. At G_{Na} = 23 pA/pF, simulated $[Na^+]_i$ increased from 12.25 mM originally to 12.77 mM which was significantly below the experimental measurement (14.6 $\pm$ 1.1 mM). On the other hand, the conductivity of the persistent Na^+ current ($GNab$) would need to be increased almost 3.5-fold from 0.0026 pA/pF to 0.0085 pA/pF in order to raise $[Na^+]_i$ to the experimental level, which was significantly greater than the observed 30% increase in this current in canine HF (25). We have obtained some preliminary measurements on the fast and persistent Na^+

currents, which suggest no significant increases in either the fast or the persistent Na^+ currents.

We hypothesized two mechanisms could potentially explain the additional increases in $[Na^+]_i$. The first mechanism could be a decrease in the Na^+ affinity of NKA (an increase in K_m). This means a higher $[Na^+]_i$ level would be required to achieve the same level of Na^+ efflux, which should be equal to Na^+ influx at steady state (21). The effect of K_m on $[Na^+]_i$, with NKA down-regulation kept at the experimentally observed levels, is shown in Fig. S5A, demonstrating an almost linear increase in $[Na^+]_i$ with increasing K_m. Experimentally measured level of $[Na^+]_i$ was matched with K_m equal to 29 mmol/L.

The second mechanism could be an increase in Na^+ influx, possibly through mechanisms such as the fast Na^+ channels, the persistent Na^+ channels and the Na^+/H^+ exchanger (NHE). However, since increases in fast and persistent Na^+ currents were not observed experimentally (not shown), they were not considered as plausible explanations. On the other hand, increased Na^+ influx through NHE due to a decreased pH_i (see Fig. S5B) could cause an $[Na^+]_i$ increase to the experimentally observed level. This was later confirmed in our experiments, where a tendency towards acidosis was observed in KO cardiomyocytes (pH_i: 6.91 ± 0.07 *v.s.* 7.19 ± 0.08 in FF).

Intracellular pH regulation

A previously developed model of intracellular pH regulation for rat ventricular myocytes (26) was introduced into the FF, 4-week and 7-week KO models. Fluxes through the Na^+/bicarbonate cotransporter and anion exchanger were set to zero in all three models, since all our experiments were conducted using bicarbonate-free external perfusion solutions containing HEPEs. Extracellular ion concentrations and pH were adjusted according to the experimental setup (see Materials and Methods). To fit the parameters for the Na^+/H^+ exchanger (NHE), we made use of the fact that total Na^+ influx and efflux per cardiac cycle must be balanced at steady state. Specifically, we first estimated the integral (over one cardiac cycle) of the Na^+ efflux through NKA and Na^+ influx through non-NHE channels in the FF and 7-week KO models by running the models, with $[Na^+]_i$ set to be constant at the experimentally measured value (FF: 9.6 mmol/L , 7-week KO: 14.6 mmol/L) and with the parameterized Ca^{2+} handling components (outlined below). The integral of the Na^+ influx through NHE in each model was then taken as the difference between the integrals of Na^+ efflux and non-NHE Na^+ influx. Since the rate of Na^+ influx through NHE does not change significantly during each cardiac cycle, it could then be approximated from the calculated integral (FF model: 0.0047 $\mu mol \cdot L^{-1} \cdot ms^{-1}$ and 7-week KO model: 0.051 $\mu mol \cdot L^{-1} \cdot ms^{-1}$). Finally, the affinity of NHE to proton (K_i = 0.411 μmol/L in all three models) and the hill coefficient (nh = 2.905 in all three models) were fitted to the above estimated Na^+ influx rates, at the experimentally observed pH_i levels in the FF and 7-week KO models.

Intracellular acidosis in the 7-week KO model was induced by the introduction of an acid flux from an intracellular acid-producing source (J_{acid} was set to 0.045 $\mu mol \cdot L^{-1} \cdot ms-1$), which could be attributed to compromised metabolism such as glycolysis. To maintain charge balance, an equal amount of intracellular anion flux (J_A) was also introduced. Build-up of $[A^-]_i$ was prevented by including a constant-field sarcolemmal flux extruding A^- from the cytosol which was taken into account when calculating changes in transmembrane potential. The membrane permeability to A^- was set to be 1×10^{-7} cm/s , such that the electrogenic transmembrane flux of A^- did not result in a significant change in resting membrane potential. It was also assumed that the A^- ions extruded from the cell was rapidly transported away from the cell such that $[A^-]_o$ was approximately zero.

Parameterization of NCX, PMCA, SERCA and L-type calcium current

Previously, we described a method for parameterizing NCX, PMCA and SERCA directly using experimentally measured $[Ca^{2+}]_i$ transients in the presence of caffeine and during field stimulations (10), provided that Ca^{2+} fluxes through NCX and PMCA are functions of cytosolic Ca^{2+} concentrations. In the current model, NCX and PMCA respond to sub-space (subsarcolemmal and junction spaces) Ca^{2+} concentrations. As a result, parameterization of NCX, PMCA and SERCA for the current model re-

quired solving a system of ordinary differential equations and matching the resulting decay of $[Ca^{2+}]_i$ to that measured experimentally, as explained below.

Generally speaking, the dynamics of Ca^{2+} concentrations in the cytosolic ($[Ca^{2+}]_i$), subsarcolemmal ($[Ca^{2+}]_{sl}$) and junctional spaces ($[Ca^{2+}]_{jc}$) during the later decay phase of a $[Ca^{2+}]_i$ transient can be described as:

$$\frac{d[Ca^{2+}]_i}{dt} = B_i \cdot (\frac{J_{Ca,slcyt}}{V_{cyt}} - J_{SERCA}) \tag{5}$$

$$\frac{d[Ca^{2+}]_{sl}}{dt} = B_{sl} \cdot (-\frac{J_{Ca,slcyt}}{V_{sl}} + \frac{J_{Ca,jcsl}}{V_{sl}} + J_{Casl}) \tag{6}$$

$$\frac{d[Ca^{2+}]_{jc}}{dt} = B_{jc} \cdot (-\frac{J_{Ca,jcsl}}{V_{jc}} + J_{Cajc}) \tag{7}$$

where V_{cyt}, V_{sl} and V_{jc} are the volumes of the cytosolic, subsarcolemmal and junctional spaces, respectively; J_{serca} is the rate of net uptake through SERCA; $J_{Ca,jcsl}$ and $J_{Ca,slcyt}$, calculated according to Eqs. 3-4, are the rates of Ca^{2+} diffusion from junctional space to subsarcolemmal space, and from subsarcolemmal space to cytosol, respectively; J_{Casl} and J_{Cajc} are the total fluxes of Ca^{2+} across the surface sarcolemmal membrane and the junctional membrane, respectively. Finally, B_i, B_{sl} and B_{jc} account for Ca^{2+} buffering in the cytosol, subsarcolemmal and junctional spaces and are calculated as:

$$B_i = (1 + \frac{B_{max} \cdot K_d}{(K_d + [Ca^{2+}]_i)^2})^{-1} \tag{8}$$

$$B_{sl} = (1 + \frac{B_{max} \cdot K_d}{(K_d + [Ca^{2+}]_{sl})^2})^{-1} \tag{9}$$

$$B_{jc} = (1 + \frac{B_{max} \cdot K_d}{(K_d + [Ca^{2+}]_{sl})^2})^{-1} \tag{10}$$

During the decay phase of a caffeine-induced $[Ca^{2+}]_i$ transient, J_{SERCA} in Eq. 5 is equal to zero. J_{Casl} and J_{Cajc} are the sums of Ca^{2+} fluxes through NCX and PMCA located on the surface sarcolemma and junctional membrane, respectively, and taking into account a small background Ca^{2+} flux. Given initial values of $[Ca^{2+}]_i$, $[Ca^{2+}]_{sl}$ and $[Ca^{2+}]_{jc}$, Eqs. 5-7 can thus be solved to give the time course of decay of $[Ca^{2+}]_i$. The relative contributions of NCX and PMCA were calculated as the ratio between the integrals of the simulated J_{NCX} and J_{PMCA}.

For parameterization, initial $[Ca^{2+}]_i$ was set equal to experimentally measured $[Ca^{2+}]_i$ at 100 ms post-peak during the caffeine-induced $[Ca^{2+}]_i$ transient. Initial $[Ca^{2+}]_{sl}$ and $[Ca^{2+}]_{jc}$ were first assumed to be equal to $[Ca^{2+}]_i$, assuming Ca^{2+} movement across the different compartments occur on a much faster time scale than Ca^{2+} removal fluxes. Maximum NCX activity (V_{NCX}^{max}), the maximum Ca^{2+} extrusion activity through PMCA (I_{PMCA}^{max}) and the Ca^{2+} affinity of PMCA ($K_{m,PMCA}$) were parameterized to minimize the cost function, which takes into account both the difference between simulated and experimentally measured decay of $[Ca^{2+}]_i$, and the difference between the simulated and experimentally estimated contributions of NCX and PMCA. During fitting, the concentrations of $[Na^+]$ in the different compartments were set to be equal to the experimentally measured cytosolic $[Na^+]$ (FF and 4-week KO: $[Na^+]_{jc} = [Na^+]_{sl} = [Na^+]_i = 9.6$ mmol/L, 7-week KO: $[Na^+]_{jc} = [Na^+]_{sl} = [Na^+]_i = 14.6$ mmol/L).

During the decay phase of a field-stimulated $[Ca^{2+}]_i$ transient at 1 Hz, J_{SERCA} in Eq. 5 is non-zero, and V_{NCX}^{max}, I_{PMCA}^{max} and $K_{m,PMCA}$ fitted from above were treated as constants in Eqs. 5-7. The experimentally measured decay of $[Ca^{2+}]_i$ can thus be used to parameterize the maximum uptake rate of SERCA (V_{up}), its Ca^{2+} affinity ($K_{m,up}$), and the small SR Ca^{2+} leak flux (J_{leak}, assumed to be constant during fitting), with initial $[Ca^{2+}]_i$, $[Ca^{2+}]_{sl}$ and $[Ca^{2+}]_{jc}$ set equal to the experimentally measured $[Ca^{2+}]_i$ at 90 ms post-peak.

The above fitted NCX, PMCA and SERCA parameter values were then incorporated into the fitting of the L-type Ca^{2+} current, using the previously described approach (10). The conductance of the channel in the junctional membrane was set to be nine times higher than that in the sarcolemma, to be

consistent with experimentally observed differential expressions of the protein (18, 19). The integral of simulated I_{CaL} was 0.116, 0.225 and 0.263 pC/pF for the FF, 4-week KO and 7-week KO models, respectively, close to experimental values of 0.111±0.009, 0.205±0.02 and 0.243±0.015 pC/pF, respectively.

The assumption of equal initial Ca^{2+} concentrations in the subsarcolemmal, junctional and cytosolic spaces were then tested by incorporating the above parameter values into the whole-cell framework as shown in Fig S6 (A-B for FF, C-D for KO). It can be seen that during most of the decay phase of the simulated transients, $[Ca^{2+}]_{jc}$ and $[Ca^{2+}]_{sl}$ were not equal to, but were linearly related to $[Ca^{2+}]_i$. Interpolation of the linear relationship at the experimentally measured $[Ca^{2+}]_i$ level thus would give a more accurate initial $[Ca^{2+}]_{jc}$ and $[Ca^{2+}]_{sl}$ values for parameterization. Table S1 shows the initially fitted parameter values with $[Ca^{2+}]_{jc}$ and $[Ca^{2+}]_{sl}$ assumed to be equal to $[Ca^{2+}]_i$, and then with interpolated $[Ca^{2+}]_{jc}$ and $[Ca^{2+}]_{sl}$ values.

A similar approach was used for parameterization of NCX, PMCA, SERCA and the L-type Ca^{2+} current in the KO model. Since caffeine-induced $[Ca^{2+}]_i$ transient in the KO cardiomyoycytes is very small in magnitude, we chose to use experimentally measured field-stimulated $[Ca^{2+}]_i$ transient (0.5 Hz) in the presence of caffeine to parameterize NCX and PMCA for the KO. Table S1 compares the final fitted parameter values between the FF and the KO models.

During parameterization, the maximum uptake activity of SERCA (V_{up}) was found to be decreased by 58 and 80% from the FF value, at the 4-week and 7-week time points, respectively. No difference was found in the affinity of SERCA to intracellular Ca^{2+} ($K_{m,up}$), i.e. allowing $K_{m,up}$ to change between the FF, 4 and 7-week models did not improve the quality of the fit. The maximum Ca^{2+} extrusion activity through PMCA (I_{PMCA}^{max}) had 10% and 2-fold increases in the 4-week and 7-week models, respectively, and the maximum exchange rate of NCX (V_{NCX}^{max}) had 43% and 5.5-fold increases in the 4-week and 7-week models, respectively, from the corresponding FF value. These values are comparable with experimentally observed progressive increase in the expression levels of NCX and PMCA (3).

Sensitivity of $[Ca^{2+}]_i$ Transients, $[Na^+]_i$ and pH_i to NHE Parameters

We tested the sensitivity of the simulated $[Ca^{2+}]_i$ transients, $[Na^+]_i$ and pH_i to the fitted NHE parameters (K_i = 0.411 μmol/L, nh = 2.905) as follows. Crampin and Smith (27) reported a K_i value of 0.3436 μmol/L (pK_i = 6.464) and an nh value of 3.18. These values are in comparison to the study of Swietach et al. (28), where K_i and nh were found to be 0.417 μmol/L (pK_i = 6.38) and 1.933 respectively. We therefore modified K_i and nh independently to these high and low values reported in literature in all three models, and compared simulated $[Ca^{2+}]_i$ transients, $[Na^+]_i$ and pH_i levels with those obtained previously using the fitted (control) values. The results, as shown in Fig. S7-S9, demonstrated that for all three models, simulated $[Ca^{2+}]_i$ transients and $[Na^+]_i$ were insensitive to both K_i and nh values, with only small changes associated with different parameter sets. Simulated pH_i changed moderately with changing K_i values, but remained within the bounds of experimentally measured average ± standard error of mean (SEM). Simulated pH_i was most sensitive to the choice of nh value, such that decreasing nh led to a higher pH_i and vice versa. However, as the mechanisms underpinning Ca^{2+} and Na^+ homeostasis was the central focus of our study, we conclude that the specific NHE parameters do not significantly influence our analysis.

Differential Effects of NKA Down-regulation

In the addition to the aforementioned compensatory changes, NKA was also found to be down-regulated. Sensitivity analysis in Fig. S11 showed that under physiological conditions such as in the FF cardiomyocytes, moderate reductions in NKA activity may beneficial effects on systolic function by enhancing peak $[Ca^{2+}]_i$ and the size of the $[Ca^{2+}]_i$ transient. However, in the 7-week KO, the same level of reduction in NKA activity resulted in a greater increase in $[Na^+]_i$ and parallel increase in both diastolic and systolic $[Ca^{2+}]_i$. While the net increase in the size of the transient was significantly attenuated thereby reducing the beneficial effect of NKA down-regulation on systolic function, the increase in diastolic

$[Ca^{2+}]_i$ may have detrimental effects on relaxation.

External Work in the Heart

Following the approach by Suga et al. (29), the mechanical energy can be estimated from the pressure-volume (PV) loop of the heart which in turn was assumed to be rectangular. The following simple formulae were proposed by Suga et al.:

$$\text{Total work} = \text{external work} + \text{potential work} \tag{11}$$

$$\text{External work} = (\text{peak pressure} - \text{diastolic pressure}) \times \text{stroke volume} \tag{12}$$

$$\text{Potential work} = \frac{(\text{end diastolic volume} - \text{stroke volume}) \times (\text{peak pressure} - \text{diastolic pressure})}{2} \tag{13}$$

$$\text{Stroke volume} = \text{cardiac output}/\text{heart rate} \tag{14}$$

The end diastolic volume was estimated from left ventricular diastolic dimension and posterior wall diastolic thickness based on the following equation proposed by Troy et al. (30) assuming the shape of the left ventricule resembles an ellipsoid:

$$\text{LVCV} = 4/3\pi\frac{\text{D}_\text{d}}{2} \times \frac{\text{D}_\text{d}}{2} \times \frac{2\text{D}_\text{d}}{2} \tag{15}$$

$$\text{LV(C\&W)V} = 4/3\pi(\frac{\text{D}_\text{d}}{2} + \text{WT}_\text{d}) \times (\frac{\text{D}_\text{d}}{2} + \text{WT}_\text{d}) \times (\frac{2\text{D}_\text{d}}{2} + \text{WT}_\text{d}) \tag{16}$$

$$\text{LVWV} = \text{LV(C\&W)V} - \text{LVCV} \tag{17}$$

where LVCV denotes left ventricular chamber volume, LV(C&W)V denotes left ventricular chamber and wall volume and LVWV denotes left ventricular wall volume. D_d and WT_d are the left ventricular diastolic dimension and posterior wall diastolic thickness, respectively, measured from echocardiography.

As shown in Table S2, the total mechanical work by the heart in the FF, 4-week KO and 7-week KO were 4.9, 4.7 and 2.9 mmHg·ml/beat, respectively, equivalent to 6.6×10^{-4}, 6.3×10^{-4} and 3.9×10^{-4} J/beat, respectively. Therefore, the total mechanical work was slightly reduced between FF and 4-week KO, and significantly reduced by 7 weeks.

On the other hand, simulated ATP consumption by ion transport was 38.1, 30.8, and 48.1 μM/beat. Given that the volumes of the heart muscle for the FF, 4-week KO and 7-week KO are approximately 0.11, 0.12, 0.09 ml, respectively, and that roughly 75% of the heart is occupied by myocytes (31), the total amount of ATP consumed by the heart for ion transport can be calculated to be 3.0×10^{-3}, 2.8×10^{-3} and 3.2×10^{-3} μmole/beat, which in turn are equivalent to 1.5×10^{-4}, 1.4×10^{-4} and 1.6×10^{-4} J/cycle, assuming 50 kJ/mol ATP (32).

The above analysis revealed that the energy consumption for ion transport in the FF, 4-week KO and 7-week KO are 23%, 22% and 41% of mechanical work, respectively. This indicated that although the sum of mechanical work and work for electrophysiology decreased from FF to 7-week KO, the overhead of running the heart doubled as a fraction of the output energy.

Effect of increased membrane area in 7-week KO

As mentioned previously (3), LV hypertrophy was not observed in either the 4-week or the 7-week KO animals. Unpublished data have, however, suggested an increase in the total surface area in the 7-week KO, which resulted from increased T-tubule density. Specifically, there appeared to be newly grown longitudinal T-tubules that contained NCX but not LCCs, while transverse T-tubule organization was maintained. Since the functional roles of these new structures are still not clear, we have not included them in the 7-week KO models.

Based on the reasons above, we have kept the volume and total membrane area unchanged in the 7-week KO model. However, we have tested the effect of an increased membrane area to make sure it does not significantly alter our simulation results. To do this, we have assumed the increase in the total membrane area is due to increased sarcolemmal membrane (A_{sl}), while the area of junctional membrane (A_{jc}) remains unchanged based on the experimental observation that the new T-tubules did not contain CaV1.2 channels (LCCs). In addition, we have adjusted the maximal activities of NCX, NKA and LCCs in the different membranes such that the overall currents are the same as those observed experimentally.

Simulated Ca^{2+} dynamics are not significantly different from those obtained previously. Simulated total ATP consumption by ion transport was slightly increased, as shown in Fig. S12, due to a slightly greater consumption by NKA as the increase in As_{sl} resulted in an increase in simulated ion flux through NKA. The overall trend is still consistent with our previous conclusion that ATP consumption by ion transport is greater in the 7-week KO model than in the FF and 4-week KO models. The aforementioned increase in NKA activity also caused a slight 4% decrease in simulated $[Na^+]_i$ (13.8 mmol/L), which was still within the experimentally measured mean $\pm$ SEM (14.6 $\pm$ 1.1 mmol/L). The effects of compensatory changes on ATP consumption also followed the same qualitative trend as that obtained previously with unchanged membrane area, as shown in Fig. S13. We therefore concluded that the possible increase in the membrane area in the 7-week KO is unlikely to have a significantly effect on the main conclusions of our study.

References

[1] Andersson, K. B., J. A. K. Birkeland, A. V. Finsen, W. E. Louch, I. Sjaastad, Y. Wang, J. Chen, J. D. Molkentin, K. R. Chien, O. M. Sejersted, and G. Christensen. 2009. Moderate heart dysfunction in mice with inducible cardiomyocyte-specific excision of the Serca2 gene. *J Mol Cell Cardiol.* 47:180–187.

[2] Andersson, K. B., L. H. Winer, H. K. Mørk, J. D. Molkentin, and F. Jaisser. 2009. Tamoxifen administration routes and dosage for inducible Cre-mediated gene disruption in mouse hearts. *Transgenic Res.* .

[3] Louch, W. E., K. Hougen, H. K. Mork, F. Swift, J. M. Aronsen, I. Sjaastad, H. M. Reims, B. Roald, K. B. Andersson, G. Christensen, and O. M. Sejersted. 2010. Sodium accumulation promotes diastolic dysfunction in end-stage heart failure following Serca2 knockout. *J Physiol.* 588:465–478.

[4] Andersson, K. B., A. V. Finsen, C. Sjaland, L. H. Winer, I. Sjaastad, A. Ødegaard, W. E. Louch, Y. Wang, J. Chen, K. R. Chien, O. M. Sejersted, and G. Christensen. 2009. Mice carrying a conditional Serca2$^{\text{flox}}$ allele for the generation of Ca^{2+} handling-deficient mouse models. *Cell Calcium.* 46:219–225.

[5] Louch, W. E., J. Hake, G. F. Jølle, H. K. Mørk, I. Sjaastad, G. T. Lines, and O. M. Sejersted. 2010. Control of Ca^{2+} release by action potential configuration in normal and failing murine cardiomyocytes. *Biophy J.* 99:1377–1386.

[6] Mørk, H. K., I. Sjaastad, J. B. Sande, M. Periasamy, O. M. Sejersted, and W. E. Louch. 2007. Increased cardiomyocyte function and Ca^{2+} transients in mice during early congestive heart failure. *J Mol Cell Cardiol.* 43:177–186.

[7] Mørk, H. K., I. Sjaastad, O. M. Sejersted, and W. E. Louch. 2009. Slowing of cardiomyocyte Ca^{2+} release and contraction during heart failure progression in postinfarction mice. *Am J Physiol Heart Circ Physiol.* 296:H1069–H1079.

[8] Swift, F., N. Tovsrud, U. H. Enger, I. Sjaastad, and O. M. Sejersted. 2007. The Na^+/K^+-ATPase α_2-isoform regulates cardiac contractility in rat cardiomyocytes. *Cardiovasc Res.* 75:109–117.

[9] Li, L., W. E. Louch, S. A. Niederer, K. B. Andersson, G. Christensen, O. M. Sejersted, and N. P. Smith. 2010. Calcium dynamics in the ventricular myocytes of SERCA2 KO mice: a modelling study. *Biophys J.* 100:332–331.

[10] Li, L., S. A. Niederer, W. Idigo, Y. H. Zhang, P. Swietach, B. Casadei, and N. P. Smith. 2010. A mathematical model of the murine ventricular myocyte: a data-driven biophysically based approach applied to mice overexpressing the canine NCX isoform. *Am J Physiol Heart Circ Physiol.* 299:H1045–1063.

[11] Shannon, T. R., F. Wang, J. Puglisi, C. Weber, and D. M. Bers. 2004. A mathematical treatment of integrated Ca dynamics within the ventricular myocyte. *Biophys J.* 87:3351–3371.

[12] Page, E., and M. Surdyk-Droske. 1979. Distribution, surface density, and membrane area of diadic junctional contacts between plasma membrane and terminal cisterns in mammalian ventricle. *Circulation Research.* 45:260–267.

[13] O'Connell, T. D., S. Ishizaka, A. Nakamura, P. M. Swigart, M. Rodrigo, G. L. Simpson, S. Cotecchia, D. G. Rokosh, W. Grossman, E. Foster, and P. C. Simpson. 2003. The α_1A/C- and α_1B-adrenergic receptors are required for physiological cardiac hypertrophy in the double-knockout mouse. *J Clin Invest.* 111:1783–1791.

[14] Jafri, M. S., J. J. Rice, and R. L. Winslow. 1998. Cardiac Ca^{2+} dynamics: The roles of ryanodine receptor adaptation and sarcoplasmic reticulum load. *Biophys J.* 74:1149–1168.

[15] Berry, R. G., S. Despa, W. Fuller, D. M. Bers, and M. J. Shattock. 2007. Differential distribution and regulation of mouse cardiac Na^+/K^+-ATPase α_1 and α_2 subunits in T-tubule and surface sarcolemmal membranes. *Cardiovasc Res.* 73:92–100.

[16] Despa, S., F. Brette, O. C.H., and D. M. Bers. 2003. Na/Ca exchange and Na/K-ATPase function are equally concentrated in transverse tubules of rat ventricular myocytes. *Biophys J.* 85:3388–3396.

[17] Yang, Z., C. Pascarel, D. S. Steele, K. Komukai, F. Brette, and C. H. Orchard. 2002. Na^+-Ca^{2+} exchange activity is localized in the T-tubules of rat ventricular myocytes. *Circ Res.* 91:315–322.

[18] Scriven, D. R. L., P. Dan, and E. D. W. Moore. 2000. Distribution of proteins implicated in excitation-contraction coupling in rat ventricular myocytes. *Biophys J.* 79:2682–2691.

[19] Kawai, M., M. Hussain, and C. H. Orchard. 1999. Excitation-contraction coupling in rat ventricular myocytes after formamide-induced detubulation. *Am J Physiol Heart Circ Physiol.* 277:H603–H609.

[20] Brette, F., and C. H. Orchard. 2006. Density and sub-cellular distribution of cardiac and neuronal sodium channel isoforms in rat ventricular myocytes. *Biochem Biophys Res Commun.* 348:1163 – 1166.

[21] Despa, S., M. A. Islam, S. M. Pogwizd, and D. M. Bers. 2002. Intracellular $[Na^+]$ and Na^+ pump rate in rat and rabbit ventricular myocytes. *J Physiol.* 539:133–143.

[22] Stimers, J. R., S. Liu, and T. A. Kinard. 1993. Effect of Nai on activity and voltage dependence of the Na/K pump in adult rat cardiac myocytes. *J Membr Biol.* 135:39–47.

[23] Han, F., J. Bossuyt, S. Despa, A. L. Tucker, and D. M. Bers. 2006. Phospholemman phosphorylation mediates the protein kinase C-dependent effects on Na^+/K^+ pump function in cardiac myocytes. *Circ Res.* 99:1376–1383.

[24] Balser, J. R. 2001. The cardiac sodium channel: Gating function and molecular phamacology. *Journal of Molecular and Cellular Cardiology*. 33:599–613.

[25] Maltsev, V. A., N. Silverman, H. N. Sabbah, and A. I. Undrovinas. 2007. Chronic heart failure slows late sodium current in human and canine ventricular myocytes: Implications for repolarization variability. *European Journal of Heart Failure*. 9:219–227.

[26] Niederer, S. A., and N. P. Smith. 2007. A mathematical model of the slow force response to stretch in rat ventricular myocytes. *Biophys J.* 92:4030–4044.

[27] Crampin, E. J., and N. P. Smith. 2006. A dynamic model of excitation-contraction coupling during acidosis in cardiac ventricular mocytes. *Biophys J.* 90:3074–3090.

[28] Swietach, P., and R. D. Vaughan-Jones. 2005. Relationship between intracellular pH and proton mobility in rat and guinea-pig ventricular myocytes. *The Journal of Physiology*. 566:793–806.

[29] Suga, H. 1979. Total mechanical energy of a ventricle model and cardiac oxygen consumption. *American Journal of Physiology - Heart and Circulatory Physiology*. 236:H498–H505.

[30] Troy, B. L., J. Pombo, and C. E. Rackley. 1972. Measurement of left ventricular wall thickness and mass by echocardiography. *Circulation*. 45:602–611.

[31] Vliegen, H. W., A. Van der Laarse, C. J. Cornelisse, and F. Eulderink. 1991. Myocardial changes in pressure overload-induced left ventricular hypertrophy. *European Heart Journal*. 12:488–494.

[32] Gibbs, C. L., and D. S. Loiselle. 2001. Cardiac basal metabolism. *The Japanese Journal of Physiology*. 51:399–426.

Table S1: Fitted parameter values for NCX, PMCA and SERCA. First fit was obtained by setting initial $[Ca^{2+}]_{jc}$ and $[Ca^{2+}]_{sl}$ equal to the experimentally measured level of $[Ca^{2+}]_i$ at approximately 100 ms post-peak $[Ca^{2+}]_i$. Second fit was obtained by using the intepolated $[Ca^{2+}]_{jc}$ and $[Ca^{2+}]_{sl}$ values, according to the relationship in Fig. S6, as initial conditions.

	FF		KO	
	First fit	Second fit	First fit	Second fit
V_{NCX}^{max} (μmol·L^{-1}·ms^{-1})	1.1009	1.1591	6.4554	6.4116
I_{PMCA}^{max} (pA/pF)	0.3509	0.5644	1.1299	1.1231
$K_{m,PMCA}$ (μmol/L)	0.2544	0.3506	0.3506 (fixed)	0.3506 (fixed)
V_{up} (μmol·L^{-1}·ms^{-1})	0.35	0.35	0.07	0.07
$K_{m,up}$ (μmol/L)	0.4928	0.4928	0.4928 (fixed)	0.4928 (fixed)

Table S2: Echocardiography measurements (1) and calculations of mechanical work of the heart.

Measurements/Calculations	FF	4-week KO	7-week KO
Systolic pressure (mmHg)	90	87	88
End-diastolici pressure (mmHg)	4	10	19
Heart rate (bpm)	443	377	433
LV diastolic dimention (mm)	3.83	3.99	3.6
Posterior wall thickness diastole	0.95	0.99	0.91
Cardiac output (ml/min)	24.6	21.1	15.7
Stroke Volume (ml)	0.0555	0.0560	0.0363
External work(mmHg ml/beat)	4.77	4.31	2.50
LVCV (ml)	0.059	0.067	0.049
LVWV (ml)	0.11	0.12	0.09
Potential work (mmHg ml/beat)	0.14	0.41	0.43
Total work (mmHg ml/beat)	4.9	4.7	2.9

Table S3: Parameter definitions and values

Parameter	Definition	FF value	4wk KO	7wk KO
C_m	Specific membrane capacitance (μF/cm^2)	1.0	1.0	1.0
F	Faraday constant (C/mmol)	96.5	96.5	96.5
T	Absolute temperature (K)	310	310	310
R	Ideal gas constant (J·mol^{-1}·K^{-1})	8.314	8.314	8.314
A_{tot}	Total membrane area (cm^{-2})	1.48×10^{-4}	1.48×10^{-4}	1.48×10^{-4}
A_{jc}:A_{tot}	Ratio between junctional membrane and total membrane areas	0.19	0.19	0.19
V_{myo}	Myoplasmic volume (μL)	2.2×10^{-5}	2.2×10^{-5}	2.2×10^{-5}
V_{jc}	Junctional space volume (μL)	2.2×10^{-8}	2.2×10^{-8}	2.2×10^{-8}
V_{sl}	Subsarcolemmal space volume (μL)	4.4×10^{-7}	4.4×10^{-7}	4.4×10^{-7}
V_{JSR}	Juctional SR volume (μL)	7.7×10^{-8}	7.7×10^{-8}	7.7×10^{-8}
V_{NSR}	Network SR volume (μL)	2.31×10^{-7}	2.31×10^{-7}	2.31×10^{-7}
B_{max}	Max. buffering capacity (μmol/L)	109	109	109
Kd_{buffer}	Affinity of buffer to Ca^{2+} (μmol/L)	0.6	0.6	0.6
$CSQN_{tot}$	CSQN: total concentration in JSR (mmol/L)	50000	50000	50000
K_m^{CSQN}	CSQN: affinity to Ca^{2+} (mmol/L)	630	630	630
$K_{m,up}$	SERCA : affinity to Ca^{2+} (μmol/L)	0.430	0.430	0.430
V_{up}	SERCA: max. uptake rate (μmol·L^{-1}·ms^{-1})	0.350	0.148	0.07
V_{leak}	SR leak: rate constant (ms^{-1})	2.0×10^{-5}	3.0×10^{-5}	2.0×10^{-5}
$D_{Ca(jcsl)}$	Ca^{2+} diffusion coefficient from jc to sl(cm^{2}s^{-1})	1.64×10^{-6}	1.64×10^{-6}	1.64×10^{-6}
$D_{Ca(slcyt)}$	Ca^{2+} diffusion coefficient from sl to cytosol (cm^{2}s^{-1})	1.22×10^{-6}	1.22×10^{-6}	1.22×10^{-6}
$D_{Na(jcsl)}$	Na^{+} diffusion coefficient from jc to sl(cm^{2}s^{-1})	1.09×10^{-5}	1.09×10^{-5}	1.09×10^{-5}
$D_{Na(slcyt)}$	Ca^{2+} diffusion coefficient from sl to cytosol (cm^{2}s^{-1})	1.79×10^{-5}	1.79×10^{-5}	1.79×10^{-5}
$A_{(jcsl)}$	Area of diffusion between jc and sl (cm^2)	5.27×10^{-6}	5.27×10^{-6}	5.27×10^{-6}
$A_{(slcyt)}$	Area of diffusion between sl and cytosol (cm^2)	1.20×10^{-4}	1.20×10^{-4}	1.20×10^{-4}
$\Delta_{x(jcsl)}$	Distance of diffusion between jc and sl (μm)	0.41	0.41	0.41
$\Delta_{x(slcyt)}$	Distance of diffusion between sl and cytosol (μm)	0.45	0.45	0.45
$A_{P_{RyR}}$	P_{RyR}: Ca^{2+} release modulating constant A (ms^{-1})	-0.2	-0.2	-0.2
$B_{P_{RyR}}$	P_{RyR}: Ca^{2+} release modulating constant B (ms^{-1})	-3.0	-3.0	-3.0
k_a^+	RyR: P_{C1} - P_{O1} rate constant (μmol/L^{-4}/ms)	6.075×10^{-6}	6.075×10^{-6}	6.075×10^{-6}
k_a^-	RyR: P_{C1} - P_{O1} rate constant (μmol/L^{-4}/ms)	0.0713	0.0713	0.0713
k_b^+	RyR: P_{O1} - P_{O2} rate constant (μmol/L^{-3}/ms)	4.05×10^{-6}	4.05×10^{-6}	4.05×10^{-6}
k_b^-	RyR: P_{O2} - P_{O1} rate constant (ms^{-1})	0.965	0.965	0.965
k_c^+	RyR: P_{O1} - P_{C2} rate constant (ms^{-1})	0.009	0.009	0.009
k_c^-	RyR: P_{C2} - P_{O1} rate constant (ms^{-1})	0.0008	0.0008	0.0008
n	RyR: Ca^{2+} cooperativity parameter P_{C1} - P_{O1}	4.0	4.0	4.0
m	RyR: Ca^{2+} cooperativity parameter P_{O1} - P_{O2}	3.0	3.0	3.0
τ_{tr}	Time constant for transfer from NSR to JSR (ms)	20	20	20
V_{rel}	RyR: max. Ca^{2+} permeability (ms^{-1})	4.5	4.5	4.5
V_{NCX}^{max}	NCX: max. exchange rate (pA/pF)	1.1591	1.656	6.412
$K_{m,Cao}$	NCX: affinity to extracellular Ca^{2+} (μmol/L)	1400	1400	1400
$K_{m,Cai}$	NCX : affinity to intracellular Ca^{2+} (μmol/L)	3.6	3.6	3.6
$K_{m,Nai}$	NCX : affinity to intracellular Na^{+} (μmol/L)	12000	12000	12000
$K_{m,Nao}$	NCX : affinity to extracellular Na^{+} (μmol/L)	88000	88000	88000
k_{sat}	NCX: saturation factor	0.27	0.27	0.27
η	NCX: V-dependence factor	0.35	0.35	0.35
K_{mallo}	NCX: allosteric regulation (μmol/L)	0.0	0.0	0.0
$K_{m,PMCA}$	PMCA: affinity of the pump to Ca^{2+} (μmol/L)	0.351	0.351	0.351

Continued on next page

Table S3 – continued from previous page

Parameter	Definition	FF	4wk KO	7wk KO
I_{PMCA}^{max}	PMCA: max. pump current (pA/pF)	0.564	0.621	1.123
P_{CaL}	LCC: permeability of the channel (μL/ms)	1.9×10^{-7}	2.0×10^{-7}	2.0×10^{-7}
Φ_L	LCC: proportion of time closed in open mode	2.5	2.5	2.5
t_L	LCC: time switching between C and O states (ms)	9.0	6.0	11.0
V_L	LCC: potential when half LCC open (mV)	-5.0	-5.0	-5.0
ΔV_L	LCC: width of opening potentials (mV)	8.0	8.0	8.0
K_L	LCC: concentration at inactivation (μmol/L)	0.8	0.7	0.6
τ_L	LCC: inactivation time (ms)	400.0	600.0	400.0
a	LCC: biasing to make inactivation function of V	0.3	0.3	0.3
b	LCC: biasing to make inactivation function of V	0.4	0.4	0.4
C_1	LCC: V-dependent inactivation constant 1 (mV)	33	33	33
C_2	LCC: V-dependent inactivation constant 2 (mV)	8.2	8.2	8.2
C_3	LCC: V-dependent inactivation constant 3 (ms)	0.1	0.1	0.1
C_4	LCC: V-dependent inactivation constant 4 (mV)	40	40	40
C_5	LCC: V-dependent inactivation constant 5 (mV)	6	6	6
C_6	LCC: V-dependent inactivation constant 6 (ms)	5	5	10
C_7	LCC: V-dependent inactivation constant 7 (ms)	315	315	315
C_8	LCC: V-dependent inactivation constant 8 (mV)	30	24	26
C_9	LCC: V-dependent inactivation constant 9 (mV)	4.5	4.5	4.5
$I_{\mathrm{NKA},\alpha1}$	Maximum NKA current for α_1 isoform (pA/pF)	5.2	5.2	4.4
$I_{\mathrm{NKA},\alpha2}$	Maximum NKA current for α_2 isoform (pA/pF)	1.95	1.95	0.9
$K_{m,Ko}$	Extracellular K^+-affinity of NKA α_1 isoform (μmol/L)	1500.0	1500.0	1500.0
$K_{m,Nai,\alpha1}$	Intracellular Na^+-affinity of NKA α_1 isoform (μmol/L)	21000	21000	21000
$K_{m,Nai,\alpha2}$	Intracellular Na^+-affinity of NKA α_2 isoform (μmol/L)	21000	21000	21000
$f_{NKA,\alpha1,const1}$	Constant 1 for V-dependence of NKA α_1 isoform	0.2946	0.2946	0.2946
$f_{NKA,\alpha1,const2}$	Constant 2 for V-dependence of NKA α_1 isoform	0.0164	0.0164	0.0164
nh	Hill coeffient for Na^+ binding of NKA α_1 and α_2 isoforms	3.0	3.0	3.0
$K_{i,NHE}$	H^+-affinity allosteric regulation of NHE by intracellular H^+	0.411	0.411	0.411
nh	Hill coefficient for allosteric regulation of NHE by intracellular H^+	2.905	2.905	2.905
G_{Cab}	I_{Cab}: max. conductance of the channel (mS/μF)	0.0004	0.0004	0.0004
P_{anion}	Permeability for anion flux (cm/s)	0	0	1.0×10^{-7}
J_{acid}	Rate of intracellular acid production (μmol·L^{-1}·ms^{-1})	0	0	0.045
P_{Cl}	Rate of intracellular acid production (cm/s)	1.3×10^{-8}	1.3×10^{-8}	1.3×10^{-8}

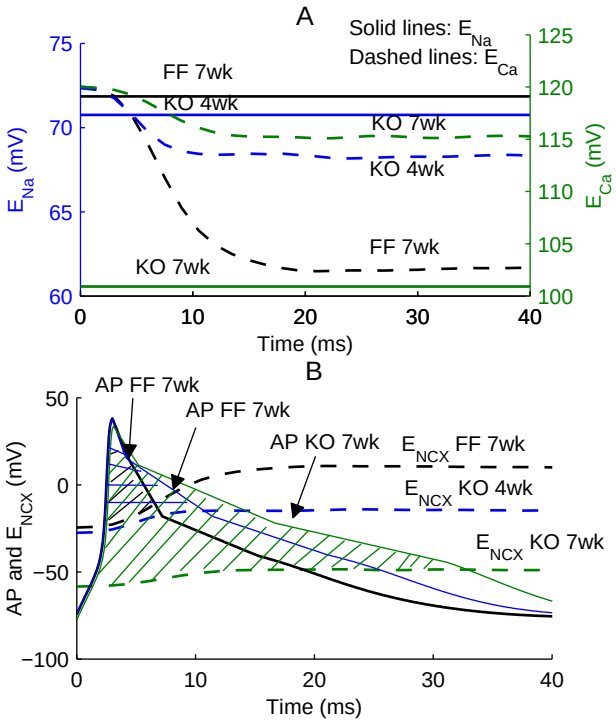

Figure S1: A: Reversal potentials for Na^+ (E_{Na}) and Ca^{2+} (E_{Ca}) estimated from the experimentally measured $[Na^+]_i$ and $[Ca^{2+}]_i$ in the FF, 4-week and 7-week KO during a cardiac cycle at 1 Hz. B: NCX reversal potential (E_{NCX}) calculated as $3\times E_{Na}$-$2\times E_{Ca}$ for the FF, 4-week and 7-week KO models, and their APs reconstructed from experimentally measured average APDs

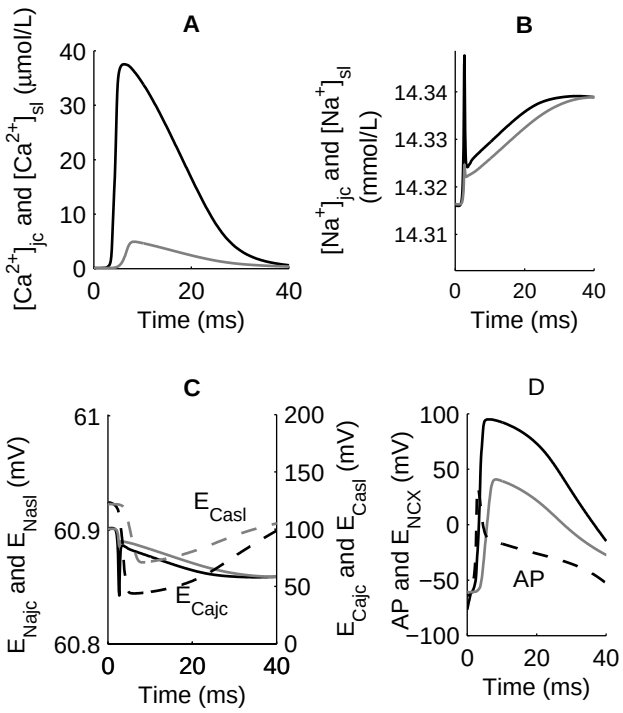

Figure S2: A: Simulated $[Ca^{2+}]_{jc}$ (black) and $[Ca^{2+}]_{sl}$ (grey) at 1 Hz in the 7-week KO model using the framework with a subsarcolemmal compartment. B. Simulated $[Na^{+}]_{jc}$ (black) and $[Na^{+}]_{sl}$ (grey) at 1 Hz in the 7-week KO model using the framework with a subsarcolemmal compartment. C: Reversal potentials for Na^{+} (E_{Na}) (solid lines) and Ca^{2+} (E_{Ca}) (dashed lines) in the junctional (black) and sarcolemmal membranes (grey), calculated from the simulated concentrations in A and B. B: NCX reversal potential (E_{NCX}) in the junctional (black) and sarcolemmal (grey) membranes, calculated as $3\times E_{Na}$-$2\times E_{Ca}$, as well as the simulated AP.

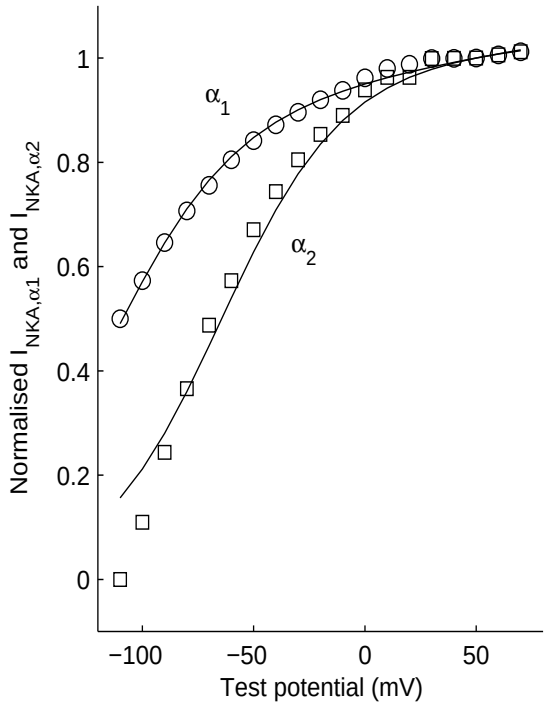

Figure S3: Experimentally measured I-V relationship of the α1 (circles) and α2 (squares) isoforms of NKA in rat ventricular myocytes (8). Superimposed (solid lines) are the fitted I-V relationship.

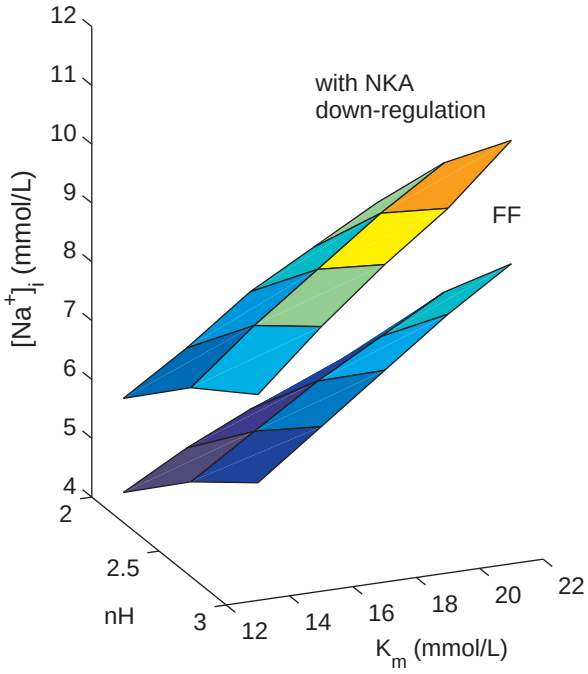

Figure S4: Simulated $[Na^+]_i$ at 1 Hz pacing frequency with various combinations of the Na^+ affinity (K_m) and the hill coefficient (nh). For FF, $I^{max}_{NKA,\alpha1}$ and $I^{max}_{NKA,\alpha2}$ were fitted to experimentally measurd $I_{NKA,\alpha1}$ and $I_{NKA,\alpha2}$, respectively (see explanation in text). The effect of NKA-downregulation was examined by adjusting $I^{max}_{NKA,\alpha1}$ and $I^{max}_{NKA,\alpha2}$ to match the experimentally observed reductions in $I_{NKA,\alpha1}$ and $I_{NKA,\alpha2}$.

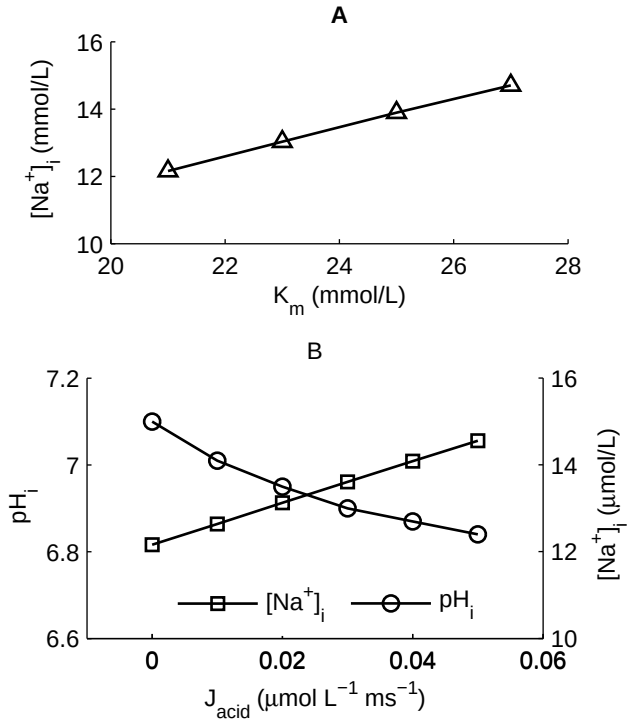

Figure S5: A. Simulated $[Na^+]_i$ at 1 Hz pacing frequency as a function ofthe Na^+ affinity of NKA. B. Simulated pH_i (circles) and $[Na^+]_i$ (squares) as a function of the size of the intracellular acid source.

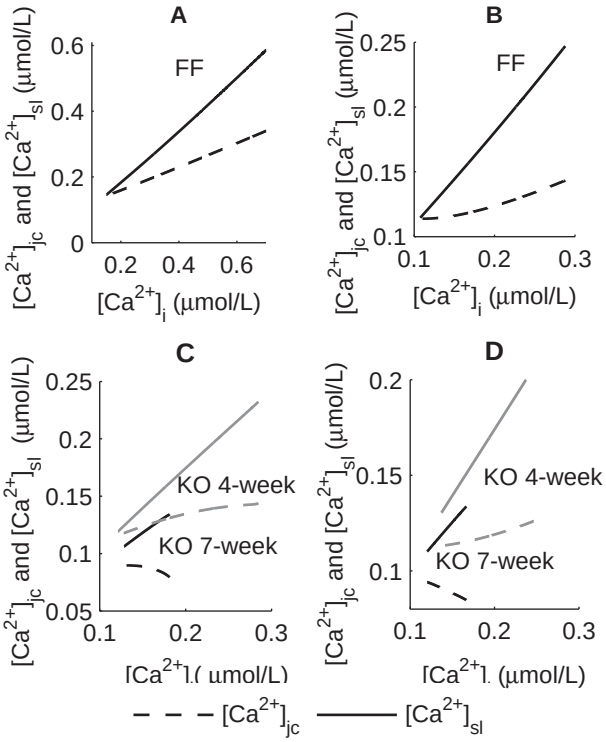

Figure S6: A. Simulated relationship between $[Ca^{2+}]_{sl}$ (solid lines), $[Ca^{2+}]_{sl}$ (dashed lines) and $[Ca^{2+}]_i$ during the decay phase of a caffeine-induced $[Ca^{2+}]_i$ transient in the FF model. B. Simulated relationship between $[Ca^{2+}]_{sl}$ (solid lines), $[Ca^{2+}]_{sl}$ (dashed lines) and $[Ca^{2+}]_i$ during the decay phase of field-stimulated $[Ca^{2+}]_i$ transient at 1 Hz in the FF model. C. Simulated relationship between $[Ca^{2+}]_{sl}$ (solid lines), $[Ca^{2+}]_{sl}$ (dashed lines) and $[Ca^{2+}]_i$ in the KO 4-week model, during the decay phase of a caffeine-induced $[Ca^{2+}]_i$ transient, and in the KO 7-week model during the decay phase of a field-stimulated $[Ca^{2+}]_i$ transient at 0.5 Hz in the presence of caffeine. D. Simulated relationship between $[Ca^{2+}]_{sl}$ (solid lines), $[Ca^{2+}]_{sl}$ (dashed lines) and $[Ca^{2+}]_i$ in the KO 4-week and KO 7-week models, during the decay phase of a field-stimulated $[Ca^{2+}]_i$ transient at 1 Hz.

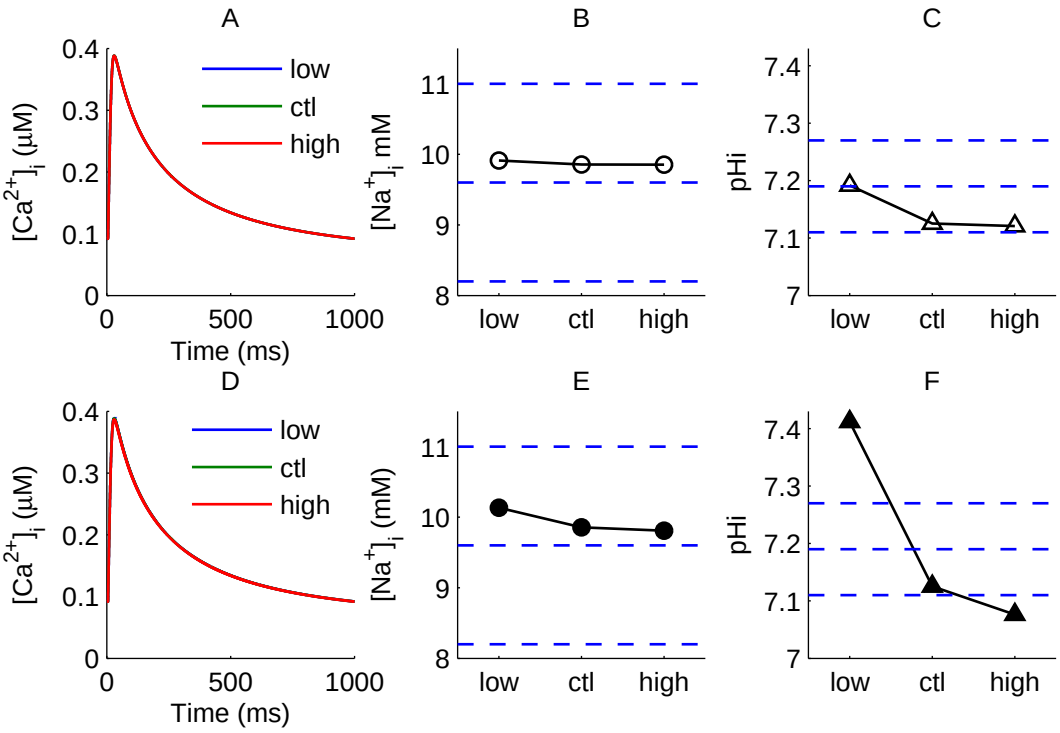

Figure S7: A-C. Simulated $[Ca^{2+}]_i$ transients, $[Na^+]_i$ and pH_i levels in the FF model, using the fitted (control or ctl) NHE K_i value, as well as the low and high values found in literature. D-F. Simulated $[Ca^{2+}]_i$ transients, $[Na^+]_i$ and pH_i levels in the FF model, using the fitted NHE nh value, as well as the low and high values found in literature. Dashed lines represent experimentally measured average $[Na^+]_i$ and pH_i, and average $\pm$ standard error of the mean (SEM).

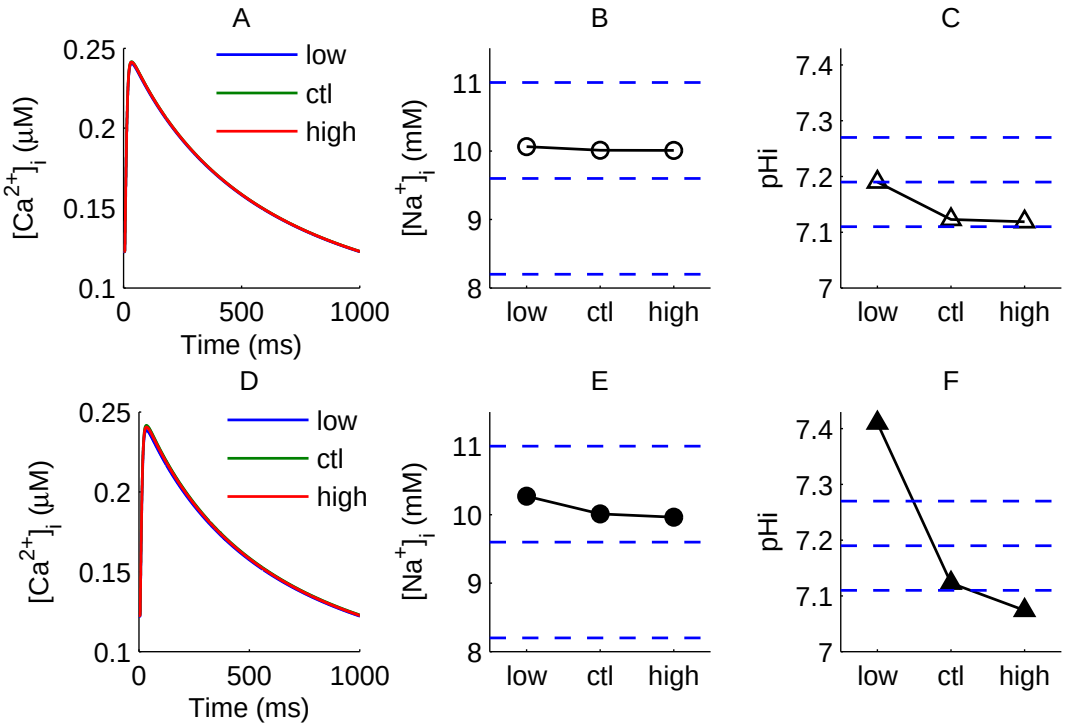

Figure S8: A-C. Simulated $[Ca^{2+}]_i$ transients, $[Na^+]_i$ and pH_i levels in the 4-week KO model, using the fitted (control or ctl) NHE K_i value, as well as the low and high values found in literature. D-F. Simulated $[Ca^{2+}]_i$ transients, $[Na^+]_i$ and pH_i levels in the 4-week KO model, using the fitted NHE nh value, as well as the low and high values found in literature. Dashed lines represent experimentally measured average $[Na^+]_i$ and pH_i, and average $\pm$ standard error of the mean (SEM).

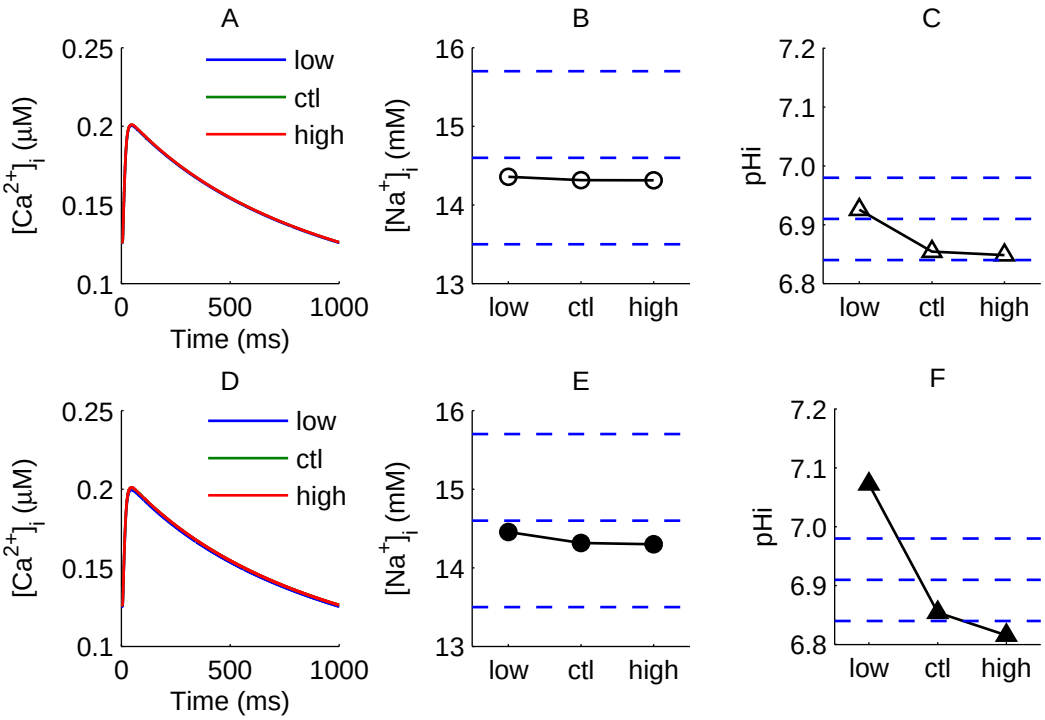

Figure S9: A-C. Simulated $[Ca^{2+}]_i$ transients, $[Na^+]_i$ and pH_i levels in the 7-week KO model, using the fitted (control or ctl) NHE K_i value, as well as the low and high values found in literature. D-F. Simulated $[Ca^{2+}]_i$ transients, $[Na^+]_i$ and pH_i levels in the 7-week KO model, using the fitted NHE nh value, as well as the low and high values found in literature. Dashed lines represent experimentally measured average $[Na^+]_i$ and pH_i, and average $\pm$ standard error of the mean (SEM).

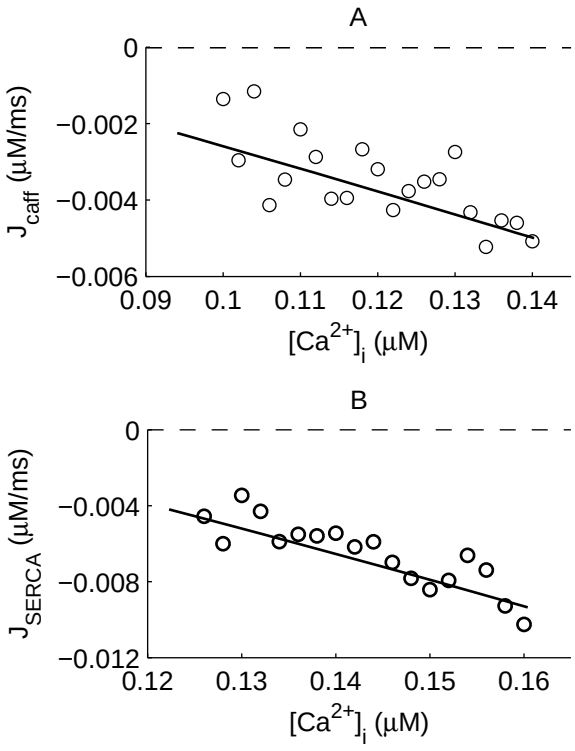

Figure S10: Fitted (solid lines) and experimentally measured (circles) Ca^{2+} fluxes vs $[Ca^{2+}]_i$ during the decay of the 1Hz $[Ca^{2+}]_i$ transient in the presence of caffeine (A) and in normal Tyrod solution (B).

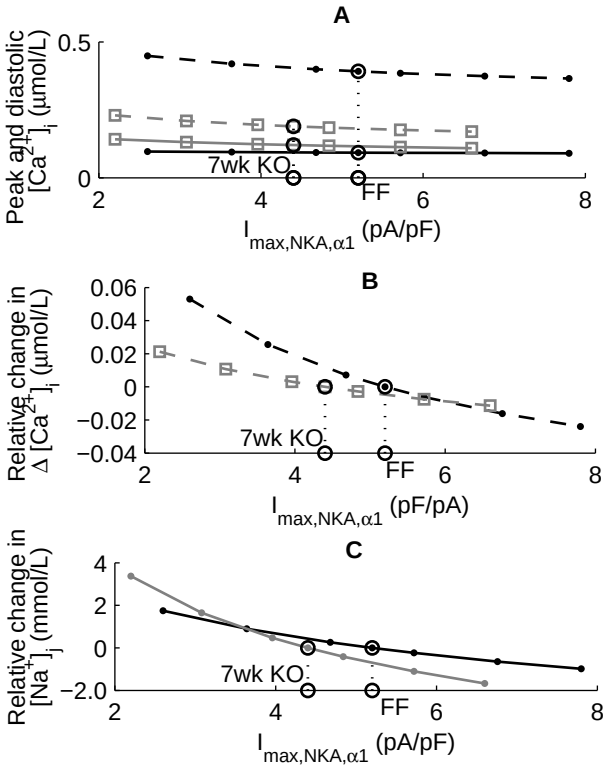

Figure S11: Simulated peak and diastolic $[Ca^{2+}]_i$ (A), $\Delta[Ca^{2+}]_i$ (B) and $[Na^+]_i$ (C) in the FF and 7-week KO models, with graded NKA downregulation.

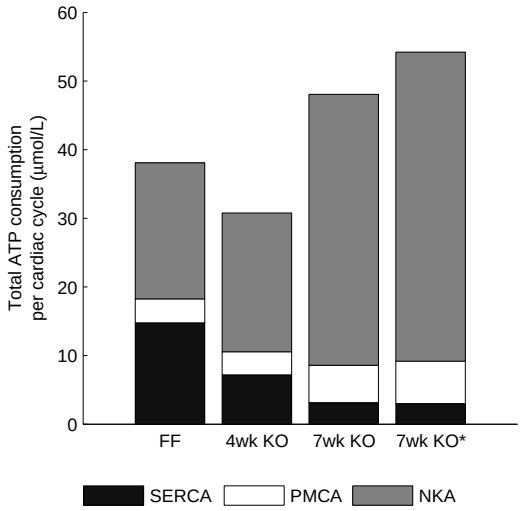

Figure S12: Comparison between simulated ATP consumption for ion transport in the FF, 4-week KO, 7-week KO, and 7-week KO* models. 7-week KO* model refers to the scenario of a greater cell membrane area attributed to an increased sarcolemmal membrane in the 7-week KO animals.

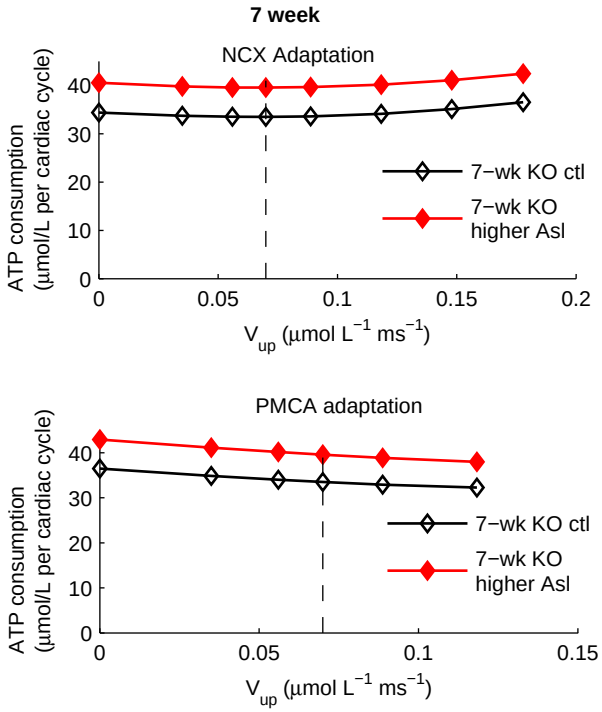

Figure S13: ATP consumption for ion transport in the case of NCX and PMCA adaptations (red) with an increased A_{sl}, compared to results with unchanged membrane areas.